JACS
JOURNAL OF THE AMERICAN CHEMICAL SOCIETY
pubs.acs.org/JACS
Article

Interfacial Reactivity-Triggered Oscillatory Lattice Strains of Nanoalloys

Zhi-Peng Wu, Dong Dinh, Yazan Maswadeh, Dominic T. Caracciolo, Hui Zhang, Tianyi Li, Jorge A. Vargas, Merry Madiou, Cailing Chen, Zhijie Kong, Zeqi Li, Huabin Zhang, Javier Ruiz Martínez, Susan S. Lu, Lichang Wang, Yang Ren, Valeri Petkov,* and Chuan-Jian Zhong*

Cite This: J. Am. Chem. Soc. 2024, 146, 35264−35274

ABSTRACT: Understanding the structure evolution of nanoalloys under reaction conditions is vital to the design of active and durable catalysts. Herein, we report an operando measurement of the dynamic lattice strains of dual-noble-metal alloyed with an earth-abundant metal as a model electrocatalyst in a working proton-exchange membrane fuel cell using synchrotron high-energy X-ray diffraction coupled with pair distribution function analysis. The results reveal an interfacial reaction-triggered oscillatory lattice strain in the alloy nanoparticles upon surface dealloying. Analysis of the lattice strains with an apparent oscillatory irregularity in terms of frequency and amplitude using time-frequency domain transformation and theoretical calculation reveals its origin from a metal atom vacancy diffusion pathway to facilitate realloying upon dealloying. This process, coupled with surface metal partial oxidation, constitutes a key factor for the nanoalloy's durability under the electrocatalytic oxygen reduction reaction condition, which serves as a new guiding principle for engineering durable or self-healable electrocatalysts for sustainable fuel cell energy conversion.

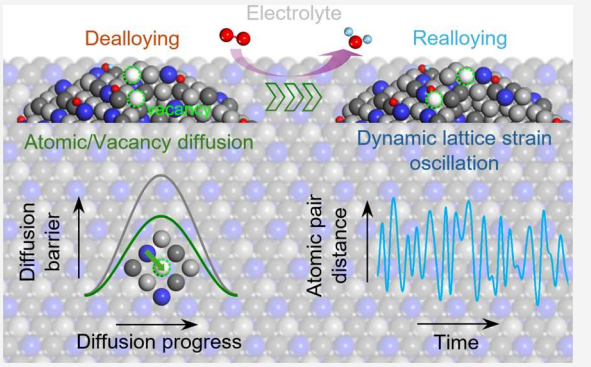

INTRODUCTION

Chemical and electrochemical interfacial reactions at a catalyst in a proton-exchange membrane fuel cell (PEMFC) play a vital role in determining the structure evolution of the catalyst under fuel cell operating conditions in correlation with electrocatalytic durability.[1] For a heterogeneous metal, alloy, or oxide catalyst system, such structure dynamics is a dynamic nonequilibrium process, which involves changes in surface adsorption, reaction sites, reactants, and products like a surface chemical clock.[2] This clock signals the dynamic durability of the catalyst at the nanoscale dimension. Given the fact that alloying of metals or mixing of different metals or oxides introduces lattice strains that define the unique structures and properties, research has mainly focused on engineering strains of alloy catalysts or electrocatalysts in a wide range of chemical reactions.[3−9] However, little is known about the chemical dynamics of the lattices under fuel cell operating conditions, particularly for nanoscale multicomponent systems where metal atom vacancy mobility differs drastically from their bulk counterparts.[7,10−12] Addressing this problem requires in situ/operando techniques to study the dynamic lattice changes in terms of both short- and long-range ordering in nanoscale systems, which presents a major challenge for most of the existing techniques. Herein, we explore the employment of operando synchrotron high-energy X-ray diffraction (HE-XRD) coupled with pair distribution function analyses (PDF) for measuring the chemical dynamics of nanoalloy catalysts under fuel cell operating conditions. A ternary nanoalloy that alloys dual-noble-metal (PtPd) with an earth-abundant Ni or Co as a model of well-defined static lattice is studied as a model system to highlight the nanoscale lattice strain evolution. In addition to providing sustainability by reducing the use of noble metals, the lower oxidation potential of Pd enhances surface passivation[13] against Pt dissolution whereas the 3d-transition base metals (Ni or Co) promote surface oxyphilicity.[14−16] The operando HE-XRD/PDF study of the nanoalloy catalysts in an working fuel cell has allowed us to reveal a previously unknown interfacial reactivity-triggered oscillatory lattice strain upon dealloying, which is linked to a realloying process of the metal elements remaining in the nanoalloy instead of redeposition. This finding is supported by the fact that the applied potentials with respect to the reduction potentials of the metal species in control experiments do not favor metal redeposition in the cycling potential window.

Received: September 10, 2024
Revised: November 20, 2024
Accepted: November 21, 2024
Published: December 10, 2024

https://doi.org/10.1021/jacs.4c12550
J. Am. Chem. Soc. 2024, 146, 35264−35274

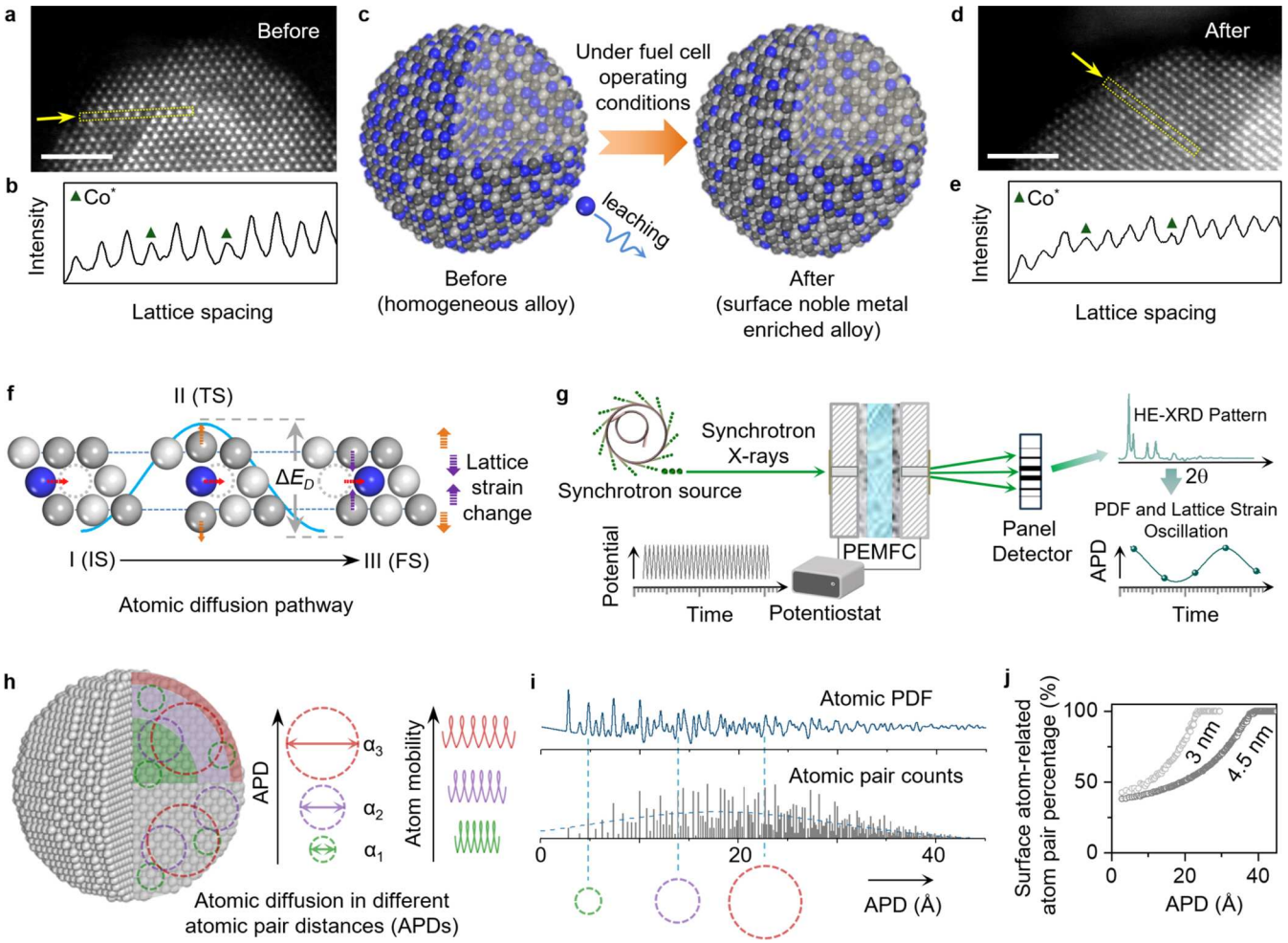

Figure 1. Dynamic lattice strains of nanoalloys in terms of atomic diffusion and atomic pair distance (APD) distribution detectable by operando HE-XRD/PDF. (a) High-resolution HAADF-STEM image, and (b) the corresponding intensity profiles of atoms for PtPdCo/C catalyst before fuel cell test. Co* denotes Co-rich atom columns. (c) Models of the nanoparticles before and after potential cycling in an operating fuel cell (light gray, gray, and blue balls denote Pt, Pd, and Co atoms, respectively). (d) HAADF-STEM image, and (e) the corresponding intensity profiles of atoms for PtPdCo/C catalyst after 2000 potential cycles. (f) Models of atomic diffusion in the lattice, causing a dynamic lattice strain change through the atomic vacancies going through (I, II, and III) an initial state (IS), transition state (TS), and final state (FS), which defines the diffusion barrier energy (ΔE_D), also known as the migration energy. (g) Illustration of the operando synchrotron X-ray diffraction and electrochemical measurement of the catalysts in a fuel cell for the dynamic PDF study. (h) Schematic illustration of atom pairs with different APD values ($\alpha_1 < \alpha_2 < \alpha_3$) and different atomic mobility, reflecting their relative enrichments in the core region (α_1), surface region (α_3), and in between (α_2). (i) PDF–APD correlation for a 4.5 nm Pt nanoparticle model: (top) the simulated PDF curve, and (bottom) the atomic pair intensity as a function of APD where the most abundant atomic pairs feature at the range of about 15–25 Å. The size variation (e.g., 4–10 nm) for real nanoparticle catalysts may slightly shift the maximum frequency position, but would not alter the general characteristic. The positions of circles in APD for illustration are drawn not to scale. (j) Plot of surface atom-related atom pair percentage as a function of the APD based on 3 and 4.5 nm sized Pt nanoparticle models. Scale bars: 2 nm (a, d).

Dealloying of base metals from Pt- or Pd-alloy catalysts in acidic electrolytes for oxygen reduction reaction (ORR) or fuel cell reactions is well established, which often involves metal ion leaching, porous structure formation, or lattice constant increase for the alloy catalyst.[17−19] However, an increasing body of studies has shown no indication of phase segregation of the metal components remaining in the alloy catalyst except for the decrease of the compressive lattice strains.[20] Traditionally, the perception of lattice strains stems largely from fresh and conditioned static states,[21−26] which does not explain the highly dynamic nature of nanoscale alloy catalysts under operating reaction conditions. A key challenge is how to determine the dynamic lattice structure under the reaction conditions. While in situ transmission electron microscopic imaging in a liquid electrochemical cell is capable of detecting metal dissolution and redeposition,[27] the atomic-scale resolution has not been achieved to pin down the dynamic lattice strain.[28,29] In this work, we employed operando HE-XRD/PDF to detect the dynamic lattice strain/parameter of nanoalloy catalysts in a working fuel cell under an accelerated durability test (ADT) condition using a triangle wave potential cycling, as recommended by the US Department of Energy.[30] The interfacial reactivity under the ADT condition triggers dealloying of the nanoalloy catalyst which is followed by a dynamic realloying process. The operando analysis of PDF peaks at different atomic pair distances (APD) reflects lattice structures from the interior to the surface regions, making this method both bulk- and surface-sensitive. The separation of PDF peaks at different APD regions allowed assessment not only of the dynamic lattice information for the nanoparticles

https://doi.org/10.1021/jacs.4c12550
J. Am. Chem. Soc. 2024, 146, 35264−35274

but also for the surface/subsurface atoms, revealing a previously unknown dynamically oscillating lattice strain. To understand the dynamic lattice strain, we analyze dealloying-induced metal atom vacancy diffusion at a frequency for atomic mobility, i.e., a jump frequency for diffusion in the lattice (see Supporting Information Note 1).[31] While typical lattice vibration frequencies can be as high as 10^{12} to 10^{13} Hz,[32] jump frequencies can be as low as sub-Hz to thousands of Hz levels depending on experimental conditions for metal as nanoparticles.[33] XRD has an intrinsic high sampling frequency ($\sim 10^{18}$ Hz) based on the typical wavelength of X-rays (~0.1 nm), but achieving a good-quality signal requires a scan rate (min to hrs.) far below that sampling frequency. To acquire long-range order information, it requires a high quality of XRD data in q space (e.g., 20−25 $Å^{-1}$) due to the signal-noise issue which inevitably sacrifices its time resolution. For such a lattice oscillation with a jump frequency, which is different from typical lattice vibration (phonon) frequency (10^{12}−10^{13} Hz),[34] simulations with different sampling time intervals (e.g., subthousands of sec to mins) showed oscillation waves with regularity and irregularity (Figure S1). A time-to-frequency domain transformation of 1 kHz-sinusoidal wave, in a sampling time (0.1 s to few mins) corresponding to the typical scan rate in HE-XRD, would produce a frequency of 0.001 to 0.01 Hz. The method is thus capable of detecting lattice oscillation dynamics despite reduced frequencies due to limitations in sampling time. In the operando measurement, the direct contribution of potential cycling to the lattice strain change could be distinguished by using a much higher potential cycling frequency (e.g., 0.125 Hz) than the sampling frequency (e.g., 0.017 Hz). Therefore, the detection of the global oscillation frequency, rather than the intrinsic metal atom diffusion, demonstrates that HE-XRD/PDF technique[35−38] is powerful for revealing the ensemble-averaged dynamic lattice structures of catalysts under the fuel cell operating conditions, which should also be applicable for studying dynamic structures of other nanomaterials and reactions.

RESULTS AND DISCUSSION

Lattice Strains and APDs. While the mobility of atoms in/on nanoparticles increases dramatically at sizes of a few nanometers (<10 nm) compared to larger-sized or bulk counterparts,[12] a key challenge is to correlate the mobility with the dynamic lattice strain under reaction conditions. We prepared and characterized both fresh and potential-cycled carbon-supported ternary nanoalloy catalysts (PtPdCo/C and PtPdNi/C). Atomically resolved images and intensity profiles from high-angle annular dark-field scanning transmission electron microscopy (HAADF-STEM) characterization confirm the face-centered-cubic (fcc) alloy structure for the fresh catalyst, which remains alloyed after potential cycling (Figures 1a−e and S2). The nanoparticle size (5.0 ± 1.0 nm) remains largely unchanged after cycling (Figure S2). Elemental mapping and line profiles of the fresh PtPdCo/C catalyst using energy dispersive spectroscopy (EDS) reveal homogeneous elemental distributions (Figure S3a−d), which is consistent with the well-defined alloy structure. The alloy integrity is retained after cycling, while there is some surface enrichment of noble metals due to the leaching of the non-noble metals (Figures 1c and S3e−h). A detailed composition analysis of the catalysts using inductively coupled plasma−optical emission spectrometry (ICP-OES) reveals that the fresh PtPdCo/C catalyst has a composition of $Pt_{22}Pd_{43}Co_{35}$ (Figure S4a). After potential cycling in the operando PEMFC, this composition shifts to $Pt_{24}Pd_{47}Co_{29}$, reflecting Co dealloying (Figure S4b). EDS elemental analysis of the samples shows that overall compositions before and after cycling closely match the ICP-OES data (Figure S4c,d). Operando HE-XRD/PDF data reveal only a minor change in the lattice parameter for the PtPdCo/C catalyst operating in the operando PEMFC, demonstrating the stability of the nanoalloy (Figure S5a,b). Under the operando PEMFC operating condition, base metal leaching during potential cycling results in increased exposure of noble metal active sites, leading to an increased electrochemically active surface area (Figure S5c,d), which is also demonstrated in a standard PEMFC (Figure S5e,f). The establishment of a stabilized or steady state after several hundred cycles demonstrates a sustained lattice strain characteristic of the nanoalloy after the initial dealloying. These findings promoted us to hypothesize that the formation of a metal vacancy upon dealloying is followed by a subsequent atomic redistribution, i.e., atomic diffusion, over nearby lattice or interstitial sites (Figure 1f). This would lead to an oscillatory lattice strain, depending on the atomic diffusion barrier energy (ΔE_D) or the diffusion coefficient (D) in terms of diffusion range (r) and time (t).

While the electrochemical potential cycling in the ADT protocol may introduce an oscillating frequency into the HE-XRD-measured PDF signals, we were able to rule out this contribution in two important ways, including performing control experiments with Pt catalysts that did not undergo dealloying (see later discussions), and using a potential cycling frequency much higher than the sampling frequency of the HE-XRD (Figure 1g). With the operando HE-XRD/PDF signals thus obtained, we focus on gaining an insight into the relative position and mobility of atoms in terms of the atom pairs and APDs (Figure 1g−i), which are defined by the physical distance between any pair of atoms in the nanoparticle. Among all possible APDs in a 4.5 nm Pt nanoparticle model, a complete count shows that the most frequently occurring ones are in the range of about 15−25 Å, displaying a bell-shaped distribution (Figure 1i). The alignment of the counted APDs (Figure 1i bottom) and the PDF curve (Figure 1i top) shows a perfect match in APD values of major PDF peaks, especially for APDs below 25 Å. Moreover, the percentage of the atomic pairs containing surface atoms increases as the APD values increase (Figures 1j and S6a). Any oscillatory lattice strain due to the dealloying-realloying linked atomic diffusion/mobility inside or on the surface of the nanoparticle is reflected by the oscillation of PDF peaks in terms of the peak positions at a given APD (Figures 1h,i and S6b). In other words, the APD value in PDF curves is correlated with the lattice strain. The amplitude and frequency of the oscillatory PDF peaks provide a measure of the lattice strains (Figure S6c,d), depending on their APD values. In contrast to a regular oscillation expected for a single crystal or facet, synchronization of multiple oscillations would lead to a dynamic oscillation with a certain degree of irregularity (Figure S6d), reflecting the combined effect of morphology and structure for the actual catalyst under the real reaction conditions. The fact that the dealloying of the catalyst in a membrane electrode assembly is weaker than in a standard electrochemical liquid cell[20] is consistent with the observation of no pronounced dealloying in the prolonged operando HE-XRD characterization of the realloying process in the fuel cell.

https://doi.org/10.1021/jacs.4c12550
J. Am. Chem. Soc. 2024, 146, 35264−35274

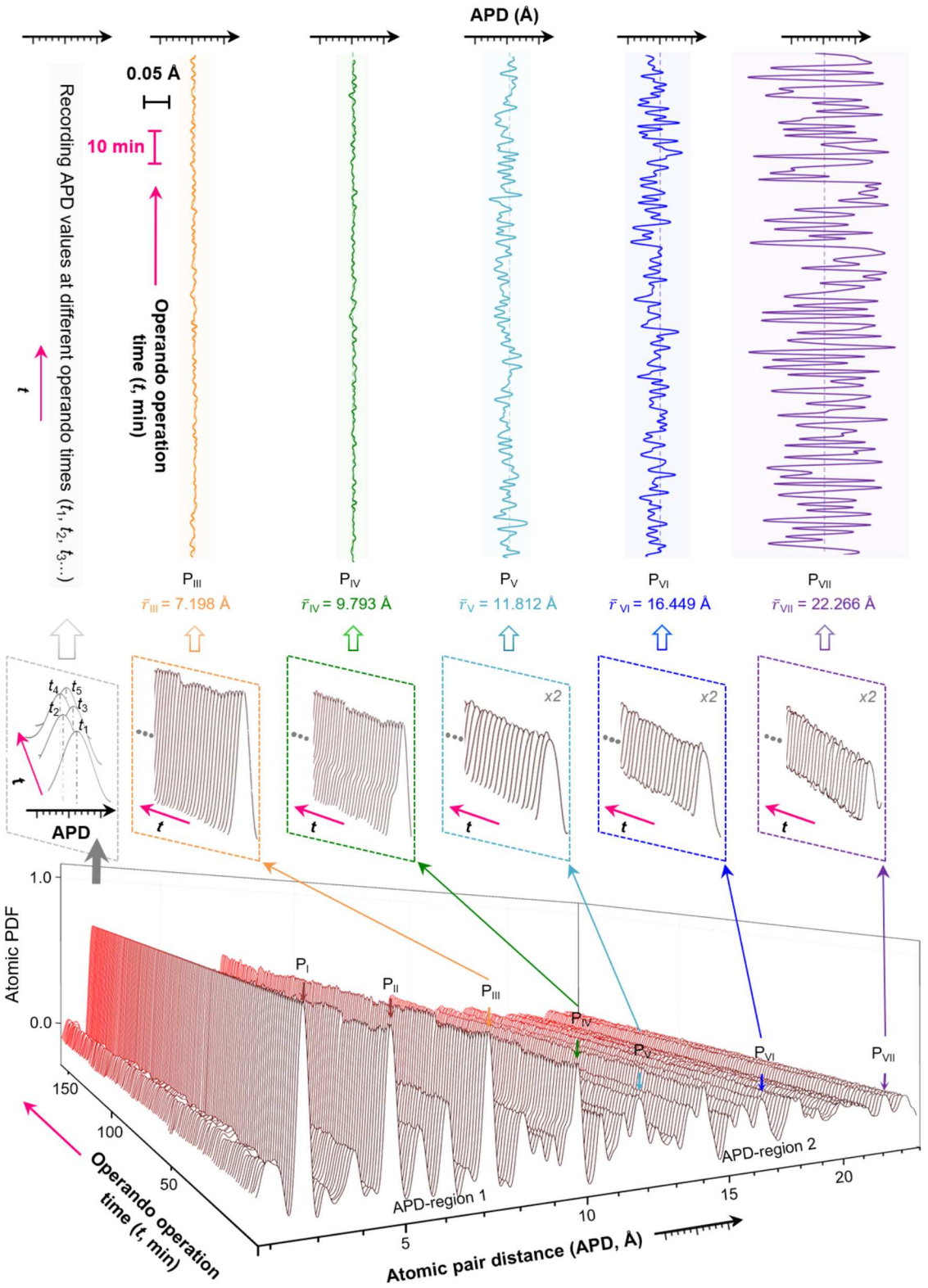

Figure 2. Operando PDF spectra showing PDF peaks at different atomic pair distances (APD) and their corresponding oscillatory characteristics. Bottom panel: The PDF waterfall spectra as a function of the operation time for PtPdCo/C catalyst in a working fuel cell during potential cycling. Middle panel: Magnified views of the indicated PDF peaks and a schematic illustration of how the APD values were precisely determined. Top panel: Plots of several PDF peaks at the indicated APDs (P_{III}–P_{VII}) versus the operation time, showing oscillatory characteristics. Dashed lines in the top panel represent the average of lattice strain oscillations for each PDF peak. The observed magnitude of the lattice oscillatory APDs (P_{III}–P_{VII}) depends strongly on the value of the APD. Other possible contributions to the origin of the oscillatory characteristic were ruled out by the following facts. First, the irregular pattern of the oscillation and time scale per cycle (~160 s) did not match with the regular pattern of the electrochemical potential cycling and the time scale per cycle (i.e., 8 s). Second, while possible oxidation/reduction reactions on the surface by the electrochemical cycling between 0.6 and 1.0 V contributed to part of the triggering force for dealloying and atomic diffusion near the surface region, there was no indication of the potential cycling-related regularity and time scale for the observed APD oscillation characteristic. Third, while there

https://doi.org/10.1021/jacs.4c12550
J. Am. Chem. Soc. 2024, 146, 35264−35274

Figure 2. continued

was a loss of a small fraction of non-noble metals (i.e., Co or Ni) (<20%) from the ternary alloy due to dealloying, there was no indication of their redeposition from the Nafion membrane that would correspond to the potential cycling-related regularity and time scale. In fact, the reduction potentials for Co/Ni ions are much more negative than the cycling potential window, which was in fact supported by the control cyclic voltammetric experiments of NiCo-alloyed Pt catalysts, showing reduction peaks at a potential of at least 0.3−0.4 V more negative than 0.6 V in the cycling potential window. Note also that the anode catalyst Pt/C is in the same path as the cathode nanoalloy catalyst (10 times Pt loading than the anode) for the penetration of X-ray and subsequent scattering in terms of diffraction, which minimizes Pt-only contribution to the observation. In fact, this was substantiated by control experiments with Pt/C catalyst only. Moreover, any possible contribution of noise to the observed lattice oscillatory characteristic was also ruled out by both control experiments with Pt/C catalysts and simulations of different noise amplitudes and frequencies (see main text and Supporting Information for further related details).

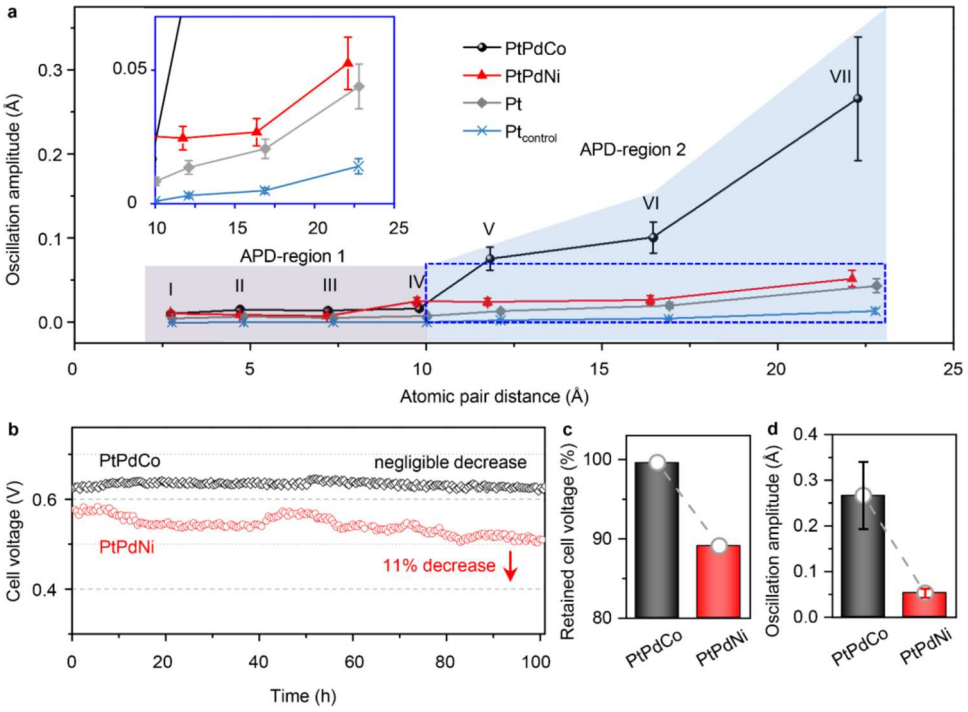

Figure 3. Amplitudes of the PDF peak position oscillations and correlation with fuel cell performance. (a) Plots of the PDF peak position oscillation amplitude vs APD derived from the operando data and the control experiments, showing different oscillation intensities for PtPdCo/C, PtPdNi/C, and Pt/C nanoparticle catalysts. $Pt_{control}$ denotes Pt/C nanoparticle powder sample measured under ambient conditions. Inset: magnified views of the dash-line indicated region at APD-region 2. The lattice oscillation amplitude is defined by the difference in the lattice strain at a specific APD. The standard deviation of the lattice strain oscillations is represented by the error bar. (b) Fuel cell stability tests at a current density of 1.0 A/cm^2 for PtPdCo/C and PtPdNi/C catalysts. (c) The retained cell voltage of PtPdCo/C and PtPdNi/C catalysts operated in a standard PEMFC after 100 h fuel cell operation. (d) The lattice strain oscillation amplitudes for Peak VII of PtPdCo/C and PtPdNi/C catalysts.

Capturing of Chemically Triggered Lattice Strain Oscillations. The chemically triggered lattice strain oscillation was captured by monitoring the PDF peak position oscillations in the operando synchrotron HE-XRD measurements under fuel-cell operating conditions (Figure S7). High-energy X-ray techniques have previously been used for catalyst characterizations in electrochemical or fuel cells,[39−42] but no prior examples have revealed oscillatory lattice strain characteristics. By analyzing the data for the catalysts in operando PEMFC (Figures 2 and S8−S11), a series of PDF peaks are shown at different APDs. In comparison, PtPdCo/C shows the highest degree of dynamic change in the amplitudes of APD oscillations, i.e., PDF peak position oscillations (Figures 3a and S9−S11). The PDF peak positions at different APDs during the potential cycling reveal persistent and irregular oscillations (Figures 2 and S9). The trend of the amplitude of lattice oscillations (PtPdCo ≫ PtPdNi > Pt) (Figure 3a) indicates the origin of the observed lattice oscillations from the nanoalloy under the reaction condition, rather than the system detection noises or possible synchrotron X-ray-induced radiation damage.

The signals are distinctively different from noise because the amplitude of the PDF peak position oscillation strongly depends on the APD value, as evidenced by direct comparisons in the three typical APD regions. The oscillations exhibit a gradual intensification from low to high APD values and maximize at ∼23 Å in APD-region 2 for PtPdCo/C (Figure 3a), which coincides with the APD value corresponding to the most abundant atomic pairs (Figure 1i). There is an increased percentage of atomic pairs containing surface/subsurface atoms with increasing APD, which is linked to the atomic diffusion near the nanoparticle−liquid−gas interface where the initial dealloying occurs, followed by the subsequent realloying. The results substantiate the necessity of analyzing large APDs beyond 10 Å. The PDF peaks in APD-region 3 (>25 Å) indicate that they are weak and thus have the propensity of being smeared by the limited resolution of the broad peaks caused by particle size/shape distribution. The PDFs in APD-

https://doi.org/10.1021/jacs.4c12550
J. Am. Chem. Soc. 2024, 146, 35264−35274

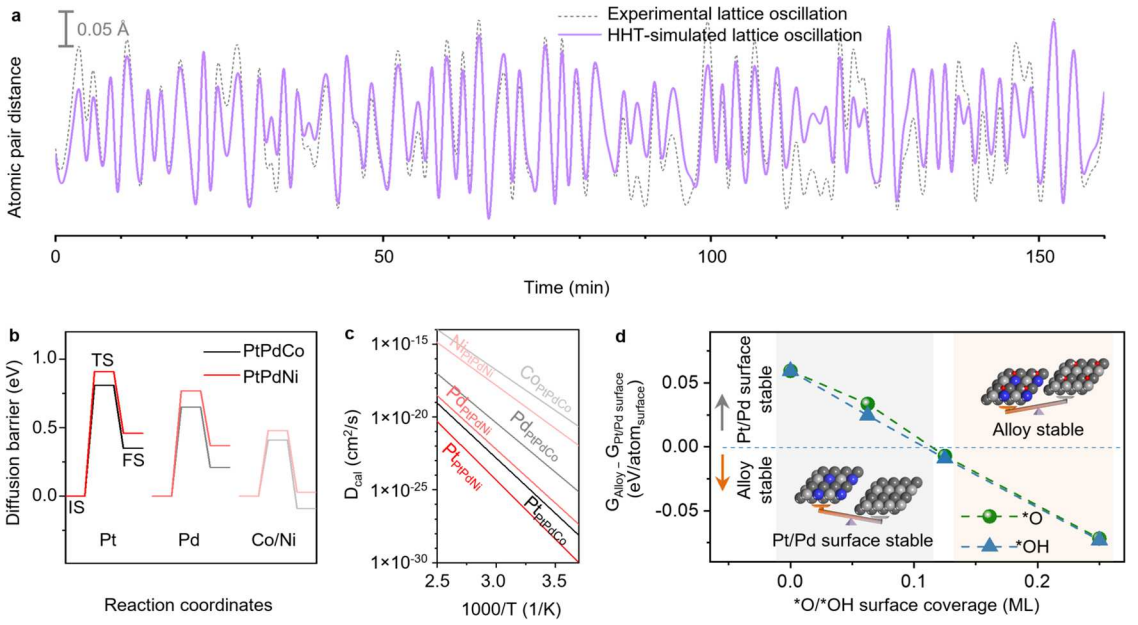

Figure 4. HHT simulations and density functional theory (DFT) calculations. (a) A comparison between the HHT-simulated lattice oscillation (purple line) and the experimentally observed lattice oscillation (dashed line). The experimental curve is determined by PDF analyses for PDF Peak VII of PtPdCo/C. The HHT-simulated curve includes the simulated IMF1 and the residual. (b) The atomic diffusion barriers of metal atoms in PtPdCo and PtPdNi alloy models. (c) Temperature dependence of the theoretically calculated diffusion coefficient (D_{cal}) of metal atoms in alloys. (d) The Gibbs free energy differences per surface atom between alloy and Pt/Pd surface models for PtPdCo. A negative value indicates the preference for the alloy structure (orange color), whereas a positive value suggests the preference for the Pt/Pd surface structure (gray color). The surface coverage of adsorbed *O and *OH species on the models is indicated by ML in terms of the fraction of monolayer coverage. The inset shows the corresponding geometric configurations at the surface region of alloy and Pt/Pd surface models with different *O/*OH surface coverage degrees. The preference for alloy or Pt/Pd surface structure is illustrated by the schematic balance.

region 2 are rich in surface information because the surface atoms account for more than 50% of the total number of atoms for a 4.5 nm nanoparticle (Figures 1j and S6a,b) in comparison with APD-region 1. For PtPdNi/C, the oscillation amplitude is higher than that of Pt/C, but much smaller than that of PtPdCo/C (Figure S11). This type of lattice strain oscillatory characteristic has also been observed for other Pt-based nanoalloy catalysts in our experiments related to this work. The noise effect can be ruled out by the fact that the same HE-XRD/PDF analyses performed under ambient conditions without apparent reactivities show significantly reduced amplitudes of APD oscillations of the PDF peaks (Figures 3a and S12). The results from the different nanoalloys and control experiments, therefore, confirm that the PDF peaks V−VII position oscillations in APD-region 2 originate from the reactivity of the nanoalloys under the fuel cell operating condition. The realloying was triggered by base metal dealloying and driven by atomic diffusion at the surface, subsurface, or interior, leading to lattice strain oscillations in different amplitudes. Such a nanoscale thermodynamics-driven realloying process is reminiscent of self-healing capability. Various control experiments were performed to substantiate our assessment of the lattice oscillation amplitude, which include controlling the particle size of the cathode catalysts to ensure a narrow size distribution of 4−5 nm and precise loading in the catalyst layers with 0.6−0.8 mg_{Pt}/cm^2 for the cathode and as low as ∼0.08 mg_{Pt}/cm^2 for the anode in all operando HE-XRD/PEMFC experiments to ensure a minimum contribution from the anode catalyst.

Implications of Chemically Triggered Oscillatory Lattice Strains. A set of binary and ternary alloys was screened to find the optimal balance of activity for ORR (Figure S13a−g). PtPdCo/C exhibits a higher current density at the same cell voltage and a higher peak power density than that of PtPdNi/C and commercial Pt/C catalysts when normalized to the noble metal mass (Figure S13h). This finding is also supported by the results of the rotating disk electrode (RDE) test in terms of mass activity (Figure S13i,j). Importantly, PtPdCo/C shows remarkable durability, as demonstrated by a negligible voltage drop (∼0.4%) after a 100-h fuel cell operation (Figure 3b), in contrast to ∼11% for PtPdNi/C. The excellent durability of the catalysts offers a clear advantage in environmental sustainability in terms of recycling and waste reduction. The retained cell voltage correlates with the oscillation amplitude, both of which are higher for PtPdCo/C than PtPdNi/C (Figure 3c,d), while PtPdCu/C[20] falls in between (Figure S13k−m). The results show an increase in the lattice strain oscillation amplitude, which is responsible for the catalyst durability under operating conditions despite the highly dynamic structure of catalysts under reaction conditions. The root cause of the dynamic structure stems from the atomic mobility or diffusion of atoms in the nanoparticles. In contrast to most of the structural characterizations for ORR and fuel cell catalysts which were carried out ex situ, we used operando techniques to investigate how the atomic mobility or diffusion plays an important role in the lattice dynamics that links the oscillation amplitude and the catalyst stability. A higher atomic diffusion mobility makes the catalyst more dynamic during the reaction, which is reflected by a higher oscillation amplitude. This dynamic behavior induces realloying to promote self-healing of the nanoalloy catalysts during the reaction, which stabilizes the catalyst by inhibiting further dealloying. A 5% drop in voltage after a 75-h durability test is observed for Pt/C, which is inferior to that of

https://doi.org/10.1021/jacs.4c12550
J. Am. Chem. Soc. 2024, 146, 35264−35274

PtPdCo/C (Figure S13n). This phenomenon arises from the significantly higher atomic mobility in PtPdCo/C, as indicated by the pronounced increase in oscillation amplitude in comparison with Pt/C.

The high durability of PtPdCo/C is also revealed by the ADT using the RDE technique in terms of catalyst composition, phase structure, and electrochemical performance (Figure S14a–f). There is a quick initial dealloying process within the first 50 cycles, which is followed by a subsequent slow realloying process (Figure S14a). A clear decrease in crystallinity index (CI) is evident after the reaction (Figure S14b,c), showing an increase in the amorphous percentage, indicative of a higher corrosion resistance.[43] The PtPdCo/C catalyst shows remarkable activity and durability for the ORR, with only 18% mass activity decay after 100,000 potential cycles (Figure S14d–f). We obtained electrochemical data directly from the operando PEMFC (Figure S5c,d) to assess the activity and durability of the catalyst. We also employed the RDE technique to quantitatively determine the electrochemically active surface area, mass activity, and specific activity, which show a gradual increase during potential cycling, reaching a steady state after a few hundred cycles (Figure S14g–i). The trend aligns well with the operando HE-XRD/PEMFC data and correlates with the behavior in the initial quick dealloying-dominated stage (see Figure S14a), leading to increased exposure of noble metal sites. However, this stage is followed by a realloying-dominated stage, leading to a slowdown of the metal leaching in comparison with the initial dealloying stage. The realloying characteristic was further substantiated by the in situ EDS analysis, showing a stable atomic composition during the operation despite the initial dealloying (Figure S14j,k). These nanoalloys have surface-enriched noble metals but retain their alloy characteristic in the operando PEMFC (Figures S2–S4), indicative of the operation of realloying and self-healing to sustain high durability.

The irregularity of lattice strain oscillation, despite its strong dependence on the nanoparticle size,[44] shape, and surface facet[45] at the solid–liquid–gas reaction interface, is analyzed using time-frequency domain transformations. To ensure clear differentiation between experimental signal and noise, we performed a detailed analysis of the observed experimental lattice oscillation data by a combination of noise subtraction from control experiments and simulation using different scaling factors for the noise, which allowed us to identify the lattice strain oscillations (Figure S15). The lattice oscillation data were analyzed by both the fast Fourier transform (FFT) and Hilbert–Huang transform (HHT) methods. HHT method[46] is used to transform the irregular lattice strain oscillation into a set of intrinsic mode function (IMF) frequencies (Figures S16 and S17). The results show that the frequencies of the IMFs for PtPdCo/C are remarkably time-dependent, substantiating the dynamic lattice strain oscillations. An average frequency can be derived from each characteristic IMF with a standard deviation. Similar results are also obtained for the other lattice strain oscillation curves (Tables S1 and S2), highlighting the order of significance of IMFs, i.e., IMF1 > IMF2 > IMF3. IMF1 reflects the most dominant oscillation characteristic, which falls in the high-frequency oscillation range (Figure 4a). The different IMFs indicate a dynamic combination of nonstationary oscillations at a given APD.

The average frequency derived from IMF1 for PtPdCo/C is higher than that for the Pt/C catalyst. A similar result is also obtained for PtPdNi/C (Tables S1 and S2). The frequencies translate to average times of 157, 161, and 183 s, respectively, for one oscillation cycle for PtPdCo/C, PtPdNi/C, and Pt/C (Table S3). The results are indeed consistent with the expectation based on the simulated oscillation waves (Figure S1). A possible contribution from electrochemical oxidation/reduction to lattice change[47] or oscillation can be ruled out because the potential cycle time (i.e., 8 s) is much shorter than the lattice oscillation cycle wavelength. Instead, the interfacial reactivity from the electrochemical oxidation/reduction contributes to part of the triggering force for dealloying and atomic diffusion near the surface region, leading to lattice oscillation. Diffusion coefficients of metals reported in the literature range from 10^{-20} to 10^{-14} cm^2/s at 80 °C.[48] Similar values were also obtained from our calculation (Figure S18). Using a typical diffusion coefficient of 10^{-18} cm^2/s, the calculated concentration gradient of vacancies across the nanoparticle is shown to be quite comparable with the time scale for the diffusion-controlled region in our operando HEXRD/PDF measurements (Figure S19). This result offers one possible explanation for the observed stable lattice oscillation, instead of gradual decay, in terms of an effective realloying process in the nanoalloy catalyst. The dynamic dealloying-realloying process is largely driven by entropy change (Figure S20). The oscillatory character is further substantiated by FFT and autocorrelation analysis methods (Figure S17b). The experimental irregular oscillation frequencies vary with time, and can be expressed by a spectrum in terms of the frequency characteristic of the corresponding APD. The oscillation amplitudes and frequencies depend not only on the APD characteristics (I to VII) but also on the nanoalloy composition (Figure S21).

Mechanistically, the dynamic lattice strain oscillation indicates the involvement of atomic diffusion in realloying upon dealloying, or atomic diffusion upon metal vacancy formation. Atomic mobility is thus assessed by DFT calculations.[49,50] Upon dealloying, a metal atom vacancy is created on the surface, which would be followed by atomic diffusion from subsurface to surface metal vacancy and vice versa. The calculations yield atomic diffusion barriers of 0.81 and 0.65 eV for Pt and Pd in the PtPdCo model, both of which are lower than the values from the PtPdNi model (0.91 and 0.77 eV for Pt and Pd) (Figure 4b and Table S4). The diffusion barrier of Co in PtPdCo is also lower than that of Ni in PtPdNi. Both base metals show lower diffusion barriers than noble metals. The results substantiate that there is an enhanced atomic diffusion in the PtPdCo alloy at the surface region. An estimation of the dealloying-induced metal atom vacancy formation energy (ΔE_{VF}) yields 0.69 eV for the surface region of PtPdCo and PtPdNi nanoalloys on the surface models. These results allow us to calculate approximately the dealloying-induced diffusion coefficients (D_{cal}) of metals in alloy models, which are plotted as a function of the reciprocal of the temperature (Figure 4c). The results indicate that the atomic diffusion in PtPdCo is enhanced compared to that in PtPdNi. The enhanced atomic diffusion is in part linked to its higher oxyphilicity, which in turn contributes to the higher durability of PtPdCo. The higher oxyphilicity is supported by the higher oxygen adsorption energy and lower oxygen dissociation energy for Co than those for Ni.[14] The dynamically oxygenated surface layer thus plays an important role in suppressing further dealloying following the initial dealloying process. Interestingly, the experimentally deter-

https://doi.org/10.1021/jacs.4c12550
J. Am. Chem. Soc. 2024, 146, 35264–35274

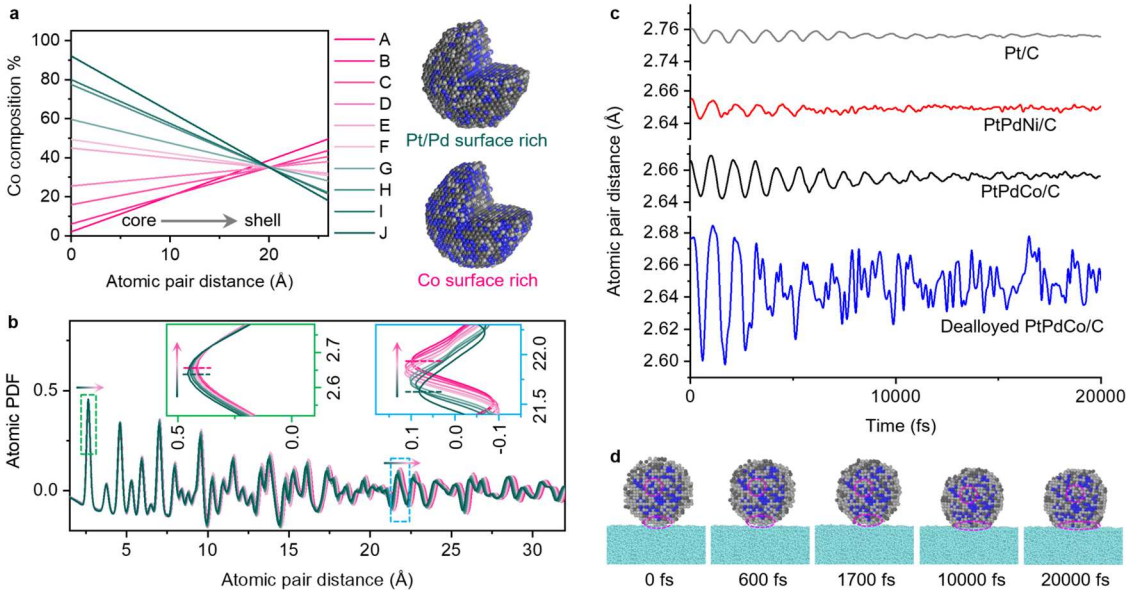

Figure 5. MD simulations of lattice strain oscillations. (a) Three-dimensional (3D) models of PtPdCo NP and radial Co distribution derived from radial probability function analysis of the models. Light gray, dark gray, and blue balls represent Pt, Pd, and Co atoms, respectively. (b) Simulated atomic PDFs based on the models with different Co distributions shown in (a). (c) MD-simulated lattice oscillations for the models of carbon-supported PtPdCo, PtPdNi, Pt, and dealloyed PtPdCo NPs. (d) Snapshots of the cross-section view of the dealloyed PtPdCo/C model during the time progress in the MD simulations.

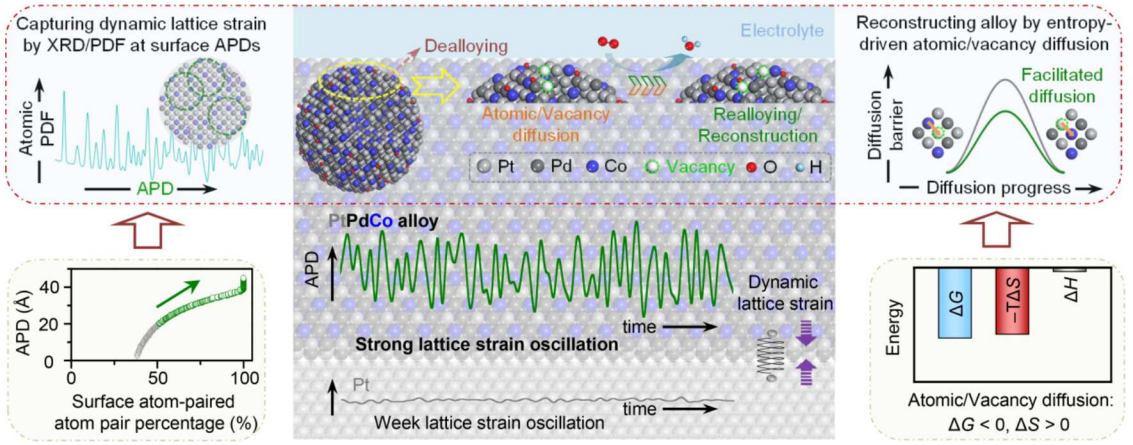

Figure 6. Schematic illustrations of experimental capturing and theoretical consideration of oscillatory lattice strain oscillations under fuel cell operating conditions. Left panel: The oscillatory lattice strain oscillation is measured by operando HE-XRD/PDF technique. The relationship between APD in atomic PDFs and the surface atom-containing atom pair percentage is exemplified by a 4.5 nm nanoparticle model. At APDs greater than 20 Å, the PDF peaks contain structural information from at least 50% of the surface atom-related atom pairs. Middle panel: Formation of atomic vacancies upon dealloying of Co from PtPdCo alloy at the initial stage, followed by the realloying/reconstruction process driven by the metal atom vacancy diffusion. Other processes such as interfacial dissolution and redeposition during the reaction are omitted for simplicity of the illustration. The surface in the nanoparticle model is partially covered by oxygenated species (*O and *OH). Light gray, dark gray, blue, red, and light blue balls represent Pt, Pd, Co, O, and H atoms, respectively. The green dotted circle represents a metal atom vacancy. Note that the sharp contrast between the weak oscillation and narrow distribution of the lattice strains for Pt nanoparticles and the strong oscillations and broad distributions of the lattice strains for PtPdCo nanoalloys is also shown in Figure S33. Right panel: The realloying/reconstruction of the nanoalloy is linked to the metal atom vacancy diffusion process, which is entropy-driven and thermodynamically favorable. The facilitated atomic diffusion is linked to strong lattice strain oscillations in the nanoalloy.

mined diffusion coefficients (D_{exp}) derived from the lattice strain oscillation analyses fall in between the theoretically calculated results (Figure S18).

The high durability of the nanoalloy catalysts is also substantiated by considering the thermodynamic stability in terms of Pt/Pd surface or alloy structures. While the Pt/Pd surface structure may be more stable for the PtPdCo model in the absence of any surface-adsorbed species, the balance is tilted toward the alloy models under electrochemical and fuel cell conditions, where *O and *OH species are adsorbed on the catalyst surface[51] (Figure S22). This assessment is supported by consideration of entropy contribution to the free energy difference between the two models in the presence of surface oxide species (Figures 4d and S23). The dynamic surface adsorption constitutes the basis for stabilizing the nanoalloy, which undergoes dealloying and realloying under the fuel cell reaction condition before reaching a thermodynamic stable state. The adsorbed oxygen species can

https://doi.org/10.1021/jacs.4c12550
J. Am. Chem. Soc. 2024, 146, 35264−35274

dynamically oxygenate the surface/subsurface oxyphilic atoms, leading to amorphization at the surface region, which is consistent with the analysis of CI (Figure S14b,c).

To elucidate the observed lattice oscillations, we performed molecular dynamics (MD) simulations of atomic dynamics in the nanoparticle catalyst. Insights were gained into some mechanistic details in several aspects. First, in addition to verification of the well-defined ternary alloy structure (Figure S24), static models of the alloy NPs with different distributions of Pt/Pd and Co across the nanoparticle at a fixed composition ranging from Co surface-rich to Pt/Pd surface-rich structures revealed a clear dependence of PDF peak position on the elemental distribution (Figures 5a,b, and S25). With a dealloyed NP model, the simulation shows a preference for uniformly distributed Co elements over one with extensive surface noble metal enrichment (Figure S24). The results are in excellent agreement with the oscillatory APDs, showing an effective realloying of the atoms inside the alloy NP upon dealloying and the associated lattice oscillations. Second, atom movement and diffusion are revealed, which contribute to the oscillatory lattice strain. The regularity and amplitude of the APD oscillations mirror remarkably well the operando PDF data (Figures 5c and S26−S30). The PtPdCo/C exhibits the highest lattice oscillation amplitude, correlating with its superior atomic diffusion mobility. This enhanced mobility, coupled with strong realloying, contributes to the enhanced catalyst stability. The dealloyed NP exhibits a much-intensified oscillation amplitude and an intriguing dependence on the atomic vacancies and the degree of realloying (Figures 5c,d, S31 and S32, and Video S1). The findings are indicative of a dynamic realloying process during the structural evolution of the alloy NP, leading to the experimentally observed lattice oscillations. Despite some deviations of the simulated oscillation frequencies from HEXRD/PDF experiment-determined oscillation frequencies, the results underscore the capability of PDF analysis for operando capturing of the dynamic realloying process under the fuel cell operating condition. Furthermore, DFT calculations of the entropy, enthalpy, and Gibbs free energy reveal that the thermodynamically favorable metal atom vacancy diffusion is driven by the entropy change (Figures 6 and S20), responsible for lattice strain oscillation for the nanoalloys under operating conditions.

CONCLUSIONS

An oscillatory lattice strain is revealed for nanoalloy catalysts under fuel cell operating conditions, which is linked to dealloying and realloying via atomic diffusion in the nanoalloy. It is the strong lattice strain oscillation that leads to a realloying process responsible for the enhanced stability of the nanoalloys under the reaction condition. This interfacial reaction-triggered oscillatory lattice strain phenomenon is unprecedented in the literature and may serve as a springboard for designing chemical/electrochemical reaction systems involving nanoscale catalysts or materials, unlocking the door to a research frontier in alloying different dual-noble-metal alloys with other transition metals toward enhanced durability. This insight not only reveals the origin of high durability of the ternary nanoalloys in the fuel cells but also has broad implications for the design of nanoalloy and other mixed metal/metal oxide catalysts with potential self-healing properties for electrochemical energy conversion and production.

ASSOCIATED CONTENT

Supporting Information

The Supporting Information is available free of charge at https://pubs.acs.org/doi/10.1021/jacs.4c12550.

Detailed experimental and simulation sections including TEM images; HAADF-STEM elemental mapping images; HE-XRD and PDF data; lattice oscillation data; ICP results; electrochemical performance; fuel cell performance; HHT and FFT simulations; DFT calculations; MD simulations; PDF data processing and quality control; HHT frequency and amplitude analyses (PDF)

MD simulation of PtPdCo/C (MP4)

AUTHOR INFORMATION

Corresponding Authors

Valeri Petkov − *Department of Physics, Central Michigan University, Mt. Pleasant, Michigan 48859, United States;* orcid.org/0000-0002-6392-7589; Email: petko1vg@cmich.edu

Chuan-Jian Zhong − *Department of Chemistry, State University of New York at Binghamton, Binghamton, New York 13902, United States;* orcid.org/0000-0003-0746-250X; Email: cjzhong@binghamton.edu

Authors

Zhi-Peng Wu − *Department of Chemistry, State University of New York at Binghamton, Binghamton, New York 13902, United States; Advanced Membranes and Porous Materials Center, Physical Sciences and Engineering Division, King Abdullah University of Science and Technology, Thuwal 23955-6900, Saudi Arabia; KAUST Catalysis Center, Physical Sciences and Engineering Division, King Abdullah University of Science and Technology, Thuwal 23955-6900, Saudi Arabia*

Dong Dinh − *Department of Systems Science and Industrial Engineering, State University of New York at Binghamton, Binghamton, New York 13902, United States*

Yazan Maswadeh − *Department of Physics, Central Michigan University, Mt. Pleasant, Michigan 48859, United States; Material Science Division, Eurofins EAG Laboratories, Sunnyvale, California 94086, United States*

Dominic T. Caracciolo − *Department of Chemistry, State University of New York at Binghamton, Binghamton, New York 13902, United States*

Hui Zhang − *Advanced Membranes and Porous Materials Center, Physical Sciences and Engineering Division, King Abdullah University of Science and Technology, Thuwal 23955-6900, Saudi Arabia; Electron Microscopy Center, South China University of Technology, Guangzhou 510640, China*

Tianyi Li − *X-ray Science Division, Advanced Photon Sources, Argonne National Laboratory, Lemont, Illinois 60439, United States;* orcid.org/0000-0002-6234-6096

Jorge A. Vargas − *Department of Physics, Central Michigan University, Mt. Pleasant, Michigan 48859, United States; Unidad Académica de Física, Universidad Autónoma de Zacatecas, Zacatecas 98098, Mexico;* orcid.org/0000-0002-9651-8183

Merry Madiou − *Department of Chemistry, State University of New York at Binghamton, Binghamton, New York 13902, United States*

Cailing Chen − *Advanced Membranes and Porous Materials Center, Physical Sciences and Engineering Division, King Abdullah University of Science and Technology, Thuwal 23955-6900, Saudi Arabia;* orcid.org/0000-0003-2598-1354

Zhijie Kong − *Department of Chemistry, State University of New York at Binghamton, Binghamton, New York 13902, United States*

Zeqi Li − *Department of Chemistry, State University of New York at Binghamton, Binghamton, New York 13902, United States*

Huabin Zhang − *KAUST Catalysis Center, Physical Sciences and Engineering Division, King Abdullah University of Science and Technology, Thuwal 23955-6900, Saudi Arabia;* orcid.org/0000-0003-1601-2471

Javier Ruiz Martínez − *KAUST Catalysis Center, Physical Sciences and Engineering Division, King Abdullah University of Science and Technology, Thuwal 23955-6900, Saudi Arabia;* orcid.org/0000-0002-9850-7939

Susan S. Lu − *Department of Systems Science and Industrial Engineering, State University of New York at Binghamton, Binghamton, New York 13902, United States*

Lichang Wang − *Department of Chemistry and Biochemistry and the Materials Technology Center, Southern Illinois University, Carbondale, Illinois 62901, United States;* orcid.org/0000-0002-6131-3532

Yang Ren − *X-ray Science Division, Advanced Photon Sources, Argonne National Laboratory, Lemont, Illinois 60439, United States; Department of Physics, City University of Hong Kong, Kowloon 999077 Hong Kong, China;* orcid.org/0000-0001-9831-6035

Complete contact information is available at: https://pubs.acs.org/10.1021/jacs.4c12550

Notes

The authors declare no competing financial interest.

■ ACKNOWLEDGMENTS

This work was supported by the National Science Foundation (CHE 2102482, and 1566283) and the Department of Energy—Basic Energy Sciences (DE-SC0006877). Access to Beamline 11-ID-C of the Advanced Photon Source, a U.S. Department of Energy (DOE) Office of Science User Facility operated for the DOE Office of Science by Argonne National Laboratory under Contract No. DE-AC02-06CH11357, is greatly appreciated. The authors thank Dr. Y. Han from King Abdullah University of Science and Technology for helpful discussion and support. The authors also acknowledge X. Li, S. Shan, and H. Kareem for their assistance in part of materials characterization and data processing.

■ REFERENCES

(1) Gasteiger, H. A.; Markovic, N. M. Just a Dream—or Future Reality? *Science* **2009**, *324*, 48−49.

(2) Ertl, G. Reactions at surfaces: from atoms to complexity (Nobel Lecture). *Angew. Chem. Int. Ed.* **2008**, *47* (19), 3524−3535.

(3) Luo, M.; Guo, S. Strain-controlled electrocatalysis on multimetallic nanomaterials. *Nat. Rev. Mater.* **2017**, *2*, No. 17059.

(4) He, T.; Wang, W.; Shi, F.; Yang, X.; Li, X.; Wu, J.; Yin, Y.; Jin, M. Mastering the surface strain of platinum catalysts for efficient electrocatalysis. *Nature* **2021**, *598* (7879), 76−81.

(5) Wang, L.; Zeng, Z.; Gao, W.; Maxson, T.; Raciti, D.; Giroux, M.; Pan, X.; Wang, C.; Greeley, J. Tunable intrinsic strain in two-dimensional transition metal electrocatalysts. *Science* **2019**, *363*, 870−874.

(6) Cheng, W.; Zhao, X.; Su, H.; Tang, F.; Che, W.; Zhang, H.; Liu, Q. Lattice-strained metal−organic-framework arrays for bifunctional oxygen electrocatalysis. *Nat. Energy* **2019**, *4*, 115−122.

(7) Wu, Z. P.; Shan, S.; Zang, S. Q.; Zhong, C. J. Dynamic core−shell and alloy structures of multimetallic nanomaterials and their catalytic synergies. *Acc. Chem. Res.* **2020**, *53*, 2913−2924.

(8) Yao, Y.; Hu, S.; Chen, W.; Huang, Z. Q.; Wei, W.; Yao, T.; Liu, R.; Zang, K.; Wang, X. X.; Wu, G.; Yuan, W.; Yuan, T.; Zhu, B.; Liu, W.; Li, Z.; He, D.; Xue, Z.; Wang, Y.; Zheng, X.; Dong, J.; Chang, C. R.; Chen, Y.; Hong, X.; Luo, J.; Wei, S.; Li, W. X.; Strasser, P.; Wu, Y.; Li, Y. Engineering the electronic structure of single atom Ru sites via compressive strain boosts acidic water oxidation electrocatalysis. *Nat. Catal.* **2019**, *2* (4), 304−313.

(9) Podjaski, F.; Weber, D.; Zhang, S.; Diehl, L.; Eger, R.; Duppel, V.; Alarcón-Lladó, E.; Richter, G.; Haase, F.; i Morral, A. F.; Scheu, C.; Lotsch, B. V. Rational strain engineering in delafossite oxides for highly efficient hydrogen evolution catalysis in acidic media. *Nat. Catal.* **2020**, *3* (1), 55−63.

(10) Ma, W.; Xie, S.; Liu, T.; Fan, Q.; Ye, J.; Sun, F.; Jiang, Z.; Zhang, Q.; Cheng, J.; Wang, Y. Electrocatalytic reduction of CO_2 to ethylene and ethanol through hydrogen-assisted C−C coupling over fluorine-modified copper. *Nat. Catal.* **2020**, *3* (6), 478−487.

(11) Li, Z.; Li, R.; Jing, H.; Xiao, J.; Xie, H.; Hong, F.; Ta, N.; Zhang, X.; Zhu, J.; Li, C. Blocking the reverse reactions of overall water splitting on a Rh/GaN−ZnO photocatalyst modified with Al_2O_3. *Nat. Catal.* **2023**, *6* (1), 80−88.

(12) Liu, X.; Wen, X.; Hoffmann, R. Surface Activation of Transition Metal Nanoparticles for Heterogeneous Catalysis: What We Can Learn from Molecular Dynamics. *ACS Catal.* **2018**, *8* (4), 3365−3375.

(13) Li, J.; Yin, H. M.; Li, X. B.; Okunishi, E.; Shen, Y. L.; He, J.; Tang, Z. K.; Wang, W. X.; Yücelen, E.; Li, C.; Gong, Y.; Gu, L.; Miao, S.; Liu, L. M.; Luo, J.; Ding, Y. Surface evolution of a Pt−Pd−Au electrocatalyst for stable oxygen reduction. *Nat. Energy* **2017**, *2*, No. 17111.

(14) Montemore, M. M.; van Spronsen, M. A.; Madix, R. J.; Friend, C. M. O_2 Activation by Metal Surfaces: Implications for Bonding and Reactivity on Heterogeneous Catalysts. *Chem. Rev.* **2018**, *118* (5), 2816−2862.

(15) Nørskov, J. K.; Abild-Pedersen, F.; Studt, F.; Bligaard, T. Density functional theory in surface chemistry and catalysis. *Proc. Natl. Acad. Sci. U.S.A.* **2011**, *108* (3), 937−943.

(16) Yang, L.; Shan, S.; Loukrakpam, R.; Petkov, V.; Ren, Y.; Wanjala, B. N.; Engelhard, M. H.; Luo, J.; Yin, J.; Chen, Y.; Zhong, C. J. Role of support-nanoalloy interactions in the atomic-scale structural and chemical ordering for tuning catalytic sites. *J. Am. Chem. Soc.* **2012**, *134* (36), 15048−15060.

(17) Tian, X.; Zhao, X.; Su, Y. Q.; Wang, L.; Wang, H.; Dang, D.; Chi, B.; Liu, H.; Hensen, E. J. M.; Lou, X. W.; Xia, B. Y. Engineering bunched Pt-Ni alloy nanocages for efficient oxygen reduction in practical fuel cells. *Science* **2019**, *366* (6467), 850−856.

(18) Wang, X. X.; Swihart, M. T.; Wu, G. Achievements, challenges and perspectives on cathode catalysts in proton exchange membrane fuel cells for transportation. *Nat. Catal.* **2019**, *2* (7), 578−589.

(19) Zhao, Z.; Liu, Z.; Zhang, A.; Yan, X.; Xue, W.; Peng, B.; Xin, H. L.; Pan, X.; Duan, X.; Huang, Y. Graphene-nanopocket-encaged PtCo nanocatalysts for highly durable fuel cell operation under demanding ultralow-Pt-loading conditions. *Nat. Nanotechnol.* **2022**, *17* (9), 968−975.

(20) Wu, Z. P.; Caracciolo, D. T.; Maswadeh, Y.; Wen, J.; Kong, Z.; Shan, S.; Vargas, J. A.; Yan, S.; Hopkins, E.; Park, K.; Sharma, A.; Ren, Y.; Petkov, V.; Wang, L.; Zhong, C. J. Alloying−realloying enabled high durability for Pt−Pd−3d-transition metal nanoparticle fuel cell catalysts. *Nat. Commun.* **2021**, *12*, No. 859.

(21) Niu, H.; Huang, L.; Qin, Y.; Qi, R.; Mei, B.; Wu, D.; Li, F. M.; You, B.; Li, Q.; Yao, Y.; Wang, Z.; Yao, T.; Ding, S.; Guo, W.; Chen, Y.; Su, Y.; Song, F.; Xia, B. Y. Hydrogen Peroxide Spillover on

Platinum-Iron Hybrid Electrocatalyst for Stable Oxygen Reduction. *J. Am. Chem. Soc.* **2024**, *146* (32), 22650−22660.
(22) Zeng, Y.; Liang, J.; Li, C.; Qiao, Z.; Li, B.; Hwang, S.; Kariuki, N. N.; Chang, C. W.; Wang, M.; Lyons, M.; Lee, S.; Feng, Z.; Wang, G.; Xie, J.; Cullen, D. A.; Myers, D. J.; Wu, G. Regulating Catalytic Properties and Thermal Stability of Pt and PtCo Intermetallic Fuel-Cell Catalysts via Strong Coupling Effects between Single-Metal Site-Rich Carbon and Pt. *J. Am. Chem. Soc.* **2023**, *145* (32), 17643−17655.
(23) Liu, X.; Wang, Y.; Liang, J.; Li, S.; Zhang, S.; Su, D.; Cai, Z.; Huang, Y.; Elbaz, L.; Li, Q. Introducing Electron Buffers into Intermetallic Pt Alloys against Surface Polarization for High-Performing Fuel Cells. *J. Am. Chem. Soc.* **2024**, *146* (3), 2033−2042.
(24) Kong, Z.; Maswadeh, Y.; Vargas, J. A.; Shan, S.; Wu, Z. P.; Kareem, H.; Leff, A. C.; Tran, D. T.; Chang, F.; Yan, S.; Nam, S.; Zhao, X.; Lee, J. M.; Luo, J.; Shastri, S.; Yu, G.; Petkov, V.; Zhong, C. J. Origin of High Activity and Durability of Twisty Nanowire Alloy Catalysts under Oxygen Reduction and Fuel Cell Operating Conditions. *J. Am. Chem. Soc.* **2020**, *142* (3), 1287−1299.
(25) Chang, F.; Shan, S.; Petkov, V.; Skeete, Z.; Lu, A.; Ravid, J.; Wu, J.; Luo, J.; Yu, G.; Ren, Y.; Zhong, C. J. Composition Tunability and (111)-Dominant Facets of Ultrathin Platinum-Gold Alloy Nanowires toward Enhanced Electrocatalysis. *J. Am. Chem. Soc.* **2016**, *138* (37), 12166−12175.
(26) Chen, C.; Kang, Y.; Huo, Z.; Zhu, Z.; Huang, W.; Xin, H. L.; Snyder, J. D.; Li, D.; Herron, J. A.; Mavrikakis, M.; Chi, M.; More, K. L.; Li, Y.; Markovic, N. M.; Somorjar, G. A.; Yang, P.; Stamenkovic, V. R. Highly Crystalline Multimetallic Nanoframes with Three-Dimensional Electrocatalytic Surfaces. *Science* **2014**, *343*, 1339−1343.
(27) Nagashima, S.; Ikai, T.; Sasaki, Y.; Kawasaki, T.; Hatanaka, T.; Kato, H.; Kishita, K. Atomic-Level Observation of Electrochemical Platinum Dissolution and Redeposition. *Nano Lett.* **2019**, *19* (10), 7000−7005.
(28) Ross, F. M. Opportunities and challenges in liquid cell electron microscopy. *Science* **2015**, *350*, No. aaa9886.
(29) Wu, Z. P.; Zhang, H.; Chen, C.; Li, G.; Han, Y. Applications of in situ electron microscopy in oxygen electrocatalysis. *Microstructures* **2022**, *2*, No. 2022002.
(30) The U.S. Department of Energy (DOE) Fuel Cell Technologies Office (FCTO), Multi-Year Research, Development, and demonstration plan. https://www.energy.gov/sites/prod/files/2016/06/f32/fcto_myrdd_fuel_cells.pdf. (accessed November 19, 2024).
(31) Ferreyra, R. A.; Juan, A. Simulations of Lattice Vibrations in a One-Dimensional Triatomic Network. *Physchem* **2023**, *3*, 440−450.
(32) Gomer, R. Diffusion of adsorbates on metal surfaces. *Rep. Prog. Phys.* **1990**, *53*, 917−1002.
(33) Surrey, A.; Pohl, D.; Schultz, L.; Rellinghaus, B. Quantitative measurement of the surface self-diffusion on Au nanoparticles by aberration-corrected transmission electron microscopy. *Nano Lett.* **2012**, *12* (12), 6071−6077.
(34) Kumar, M.; Hemkar, M. P. Lattice vibrations and Debye-Waller factors in f.c.c. metals. *Nuovo Cimento B* **1978**, *44*, 451−468.
(35) Kong, Z.; Wu, Z. P.; Maswadeh, Y.; Yu, G.; Vargas, J. A.; Caracciolo, D.; Petkov, V.; Zang, S. Q.; Tao, L.; Wang, S.; Zhong, C. J. Self-Sustainable Lattice Strains of Morphology-Tuned Nanowires in Electrocatalysis. *ACS Catal.* **2024**, *14*, 4709−4718.
(36) Terban, M. W.; Billinge, S. J. L. Structural Analysis of Molecular Materials Using the Pair Distribution Function. *Chem. Rev.* **2022**, *122* (1), 1208−1272.
(37) Gao, F. Y.; Liu, S. N.; Ge, J. C.; Zhang, X. L.; Zhu, L.; Zheng, Y. R.; Duan, Y.; Qin, S.; Dong, W.; Yu, X.; Bao, R. C.; Yang, P. P.; Niu, Z. Z.; Ding, Z. G.; Liu, W.; Lan, S.; Gao, M. R.; Yan, Y.; Yu, S. H. Nickel−molybdenum−niobium metallic glass for efficient hydrogen oxidation in hydroxide exchange membrane fuel cells. *Nat. Catal.* **2022**, *5*, 993−1005.
(38) Craig, M. J.; García-Melchor, M. Faster hydrogen production in alkaline media. *Nat. Catal.* **2020**, *3* (12), 967−968.
(39) Benck, J. D.; Jackson, A.; Young, D.; Rettenwander, D.; Chiang, Y. M. Producing High Concentrations of Hydrogen in Palladium via Electrochemical Insertion from Aqueous and Solid Electrolytes. *Chem. Mater.* **2019**, *31* (11), 4234−4245.
(40) Redmond, E. L.; Setzler, B. P.; Juhas, P.; Billinge, S. J. L.; Fuller, T. F. In-Situ Monitoring of Particle Growth at PEMFC Cathode under Accelerated Cycling Conditions. *Electrochem. Solid-State Lett.* **2012**, *15* (5), No. B72.
(41) Fuchs, T.; Drnec, J.; Calle-Vallejo, F.; Stubb, N.; Sandbeck, D. J. S.; Ruge, M.; Cherevko, S.; Harrington, D. A.; Magnussen, O. M. Structure dependency of the atomic-scale mechanisms of platinum electro-oxidation and dissolution. *Nat. Catal.* **2020**, *3* (9), 754−761.
(42) Martens, I.; Chattot, R.; Wiegmann, T.; Fuchs, T.; Magnussen, O. M.; Dubau, L.; Maillard, F.; Drnec, J. Towards comprehensive understanding of proton-exchange membrane fuel cells using high energy x-rays. *J. Phys. Energy* **2021**, *3* (3), No. 031003.
(43) Xie, C.; Milošev, I.; Renner, F. U.; Kokalj, A.; Bruna, P.; Crespo, D. Corrosion resistance of crystalline and amorphous CuZr alloys in NaCl aqueous environment and effect of corrosion inhibitors. *J. Alloys Compd.* **2021**, *879*, No. 160464.
(44) Zhdanov, V. P.; Kasemo, B. Kinetic oscillations on nm-sized catalyst particles: oxide model. *Surf. Sci.* **2002**, *511*, 23−33.
(45) Suchorski, Y.; Zeininger, J.; Buhr, S.; Raab, M.; Stöger-Pollach, M.; Bernardi, J.; Grönbeck, H.; Rupprechter, G. Resolving multi-frequential oscillations and nanoscale interfacet communication in single-particle catalysis. *Science* **2021**, *372*, 1314−1318.
(46) Huang, N. E.; Shen, Z.; Long, S. R.; Wu, M. C.; Shih, H. H.; Zheng, Q.; Yen, N. C.; Tung, C. C.; Liu, H. H. The empirical mode decomposition and the Hilbert spectrum for nonlinear and non-stationary time series analysis. *Proc. R. Soc. London, Ser. A* **1998**, *454*, 903−995.
(47) Chattot, R.; Martens, I.; Mirolo, M.; Ronovsky, M.; Russello, F.; Isern, H.; Braesch, G.; Hornberger, E.; Strasser, P.; Sibert, E.; Chatenet, M.; Honkimaki, V.; Drnec, J. Electrochemical Strain Dynamics in Noble Metal Nanocatalysts. *J. Am. Chem. Soc.* **2021**, *143* (41), 17068−17078.
(48) Xiong, G.; Clark, J. N.; Nicklin, C.; Rawle, J.; Robinson, I. K. Atomic Diffusion within Individual Gold Nanocrystal. *Sci. Rep.* **2014**, *4*, No. 6765.
(49) Mantina, M.; Wang, Y.; Arroyave, R.; Chen, L. Q.; Liu, Z. K.; Wolverton, C. First-principles calculation of self-diffusion coefficients. *Phys. Rev. Lett.* **2008**, *100* (21), No. 215901.
(50) Lai, K. C.; Han, Y.; Spurgeon, P.; Huang, W.; Thiel, P. A.; Liu, D. J.; Evans, J. W. Reshaping, Intermixing, and Coarsening for Metallic Nanocrystals: Nonequilibrium Statistical Mechanical and Coarse-Grained Modeling. *Chem. Rev.* **2019**, *119* (11), 6670−6768.
(51) Luo, M.; Koper, M. T. M. A kinetic descriptor for the electrolyte effect on the oxygen reduction kinetics on Pt(111). *Nat. Catal.* **2022**, *5* (7), 615−623.

https://doi.org/10.1021/jacs.4c12550
J. Am. Chem. Soc. 2024, 146, 35264−35274